Electronic, magneto-optical and magneto-transport properties of the topological insulator Sb_2Te_2Se

Yulia E. Kovalenko[1,*], Michael V. Yakushev[1, 2, 3, 4], Vladimir I. Grebennikov[1], Vladimir A. Golyashov[5, 6], Vyacheslav V. Marchenkov[1,3], Milan Orlita[7], Yuri S. Ponosov[1, 3], Evgeniy I. Patrakov[1], Svetlana G. Titova[8], Robert W. Martin[4], Konstantin A. Kokh[9], Oleg E. Tereshchenko[1 ,5, 6] and Tatyana V. Kuznetsova[1, 3]

[1]M.N. Mikheev Institute of Metal Physics of UB RAS, 18 S. Kovalevskaya Str., Ekaterinburg, 620108, Russia
[2]Institute of Solid State Chemistry of UB RAS, 91 Pervomaiskaya Str., Ekaterinburg, 620990, Russia
[3]Ural Federal University, 19 Mira Str., Ekaterinburg, 620002, Russia
[4]Department of Physics, SUPA, Strathclyde University, 107 Rottenrow, Glasgow G4 0NG, UK
[5]Rzhanov Institute of Semiconductor Physics of SB RAS, 13 Ac. Lavrentieva Ave., Novosibirsk, 630090, Russia
[6] Synchrotron Radiation Facility SKIF, Boreskov Institute of Catalysis SB RAS, 630559 Kol'tsovo, Russia
[7]LNCMI, 25 Martyrs Ave., BP 166, 38042 Grenoble Cedex 9, France
[8]Institute of Metallurgy of UB RAS, 101 Amundsen Str., Ekaterinburg, 620016, Russia
[9]V.S. Sobolev Institute of Geology and Mineralogy of SB RAS, 3 Koptyuga Ave., Novosibirsk, 630090, Russia

ABSTRACT. The structural, magneto-optical and magneto-transport properties as well as the electronic band structure of the bulk crystalline topological insulator (TI) Sb_2Te_2Se, grown by the vertical Bridgman technique, were studied. The high structural quality of the grown crystals was established by X-ray diffraction and Raman spectroscopy. Angular Resolved Photoelectron Spectroscopy revealed a single Dirac cone with the Dirac point, away from the valence as well as conduction bands, 0.22 eV above the Fermi level. The magneto-transport data exhibited a distinct single frequency Shubnikov-de Haas oscillation in magnetic fields above B = 10 T. Lifshitz-Kosevich analysis of the data suggests that this oscillation originates from the Dirac-type states. A sharp fundamental absorption edge in the mid-infrared transmission spectra measured at 4.2 K demonstrated a direct bandgap of 0.377 eV located at a momentum of 0.1 Å^{-1} along the $\overline{\Gamma}-\overline{K}$ directions of the Brillouin zone. A two-band model developed for massive Dirac electrons in the bulk of topological insulators with the direct bandgap at a non-Γ point suggests hyperbolic dispersion relations for the conduction and valence bands displaying the full electron-hole symmetry. Equal magnitude of the electron and hole effective masses $m_e \approx m_h \approx 0.21m_0$ and g factors $g_e \approx g_h \approx 10$ were estimated.

I. INTRODUCTION.

Due to their exotic electronic properties, high potential for low power spintronics [1] and ultralow dissipation electronics [2] topological insulators (TIs) have sparked significant interest of the world research community. Strong spin-orbital coupling induces in TIs topologically protected surface states (TSS) with a single zero bandgap Dirac-type dispersion cone whereas in the bulk TIs remain insulator-like [3]. The Dirac fermion-based charge carrier transport, associated with TSS, is topologically protected from back-scattering and localization resulting in an ultralow dissipation. One of the requirements for the realisation of such a transport is the energy position of the Dirac point, which should be away from the bulk valence and conduction bands [4]. However, in the binary tetradymites Bi_2Se_3, Bi_2Te_3 and Sb_2Te_3, long known as thermoelectric materials, considered to be model examples of TIs, the electronic properties are not suitable for straight forward applications due to the proximity of their Dirac point to the bulk conduction and valence bands influencing the transport properties [5]. Another requirement for the ultralow dissipation transport is the position of the bulk Fermi level (E_F) which should be at the Dirac point [4,6].

Alloying the model binary TIs into multinary solid solutions was proposed for tuning the Dirac point position [6-11]. One of such solid solutions, the ternary compound Sb_2Te_2Se, was theoretically predicted and confirmed experimentally, (using angular resolved photoelectron spectroscopy, ARPES), to be a topological insulator with the Dirac point separated from the bulk bands [12,13].

Amongst a considerable number of studies on multinary solid solutions, derived from the model binary TIs by alloying, Sb_2Te_2Se has so far received a surprisingly low level of attention although this compound demonstrates a remarkable stability of its TSS and the doping level against air exposure [13]. The photoemission spectra of Sb_2Te_2Se revealed no oxidation signal after the room temperature deposition of oxygen whereas the TSS band dispersion relations remained unchanged suggesting their stability to atmospheric contamination of the surface. These make Sb_2Te_2Se a very attractive material for atmospheric applications.

*Contact author: yulya.khatchenko@mail.ru

The stability of TSS in Sb_2Te_2Se against extrinsic doping has been demonstrated using Shubnikov–de Haas oscillations (SdH) [14]. After doping with Sn, changing the bulk conductivity from *n*- to *p*-type, the Berry phase value (an important parameter to identify the topological nature of materials) remained non-trivial, which demonstrates that the bulk doping does not damage TSS in Sb_2Te_2Se and can be used as an effective method for tuning E_F with respect to the Dirac point. Such a position is often determined using ARPES [12,13]. However, this method is surface sensitive and therefore can be affected by a band bending due to the surface charge collection making ARPES not quite reliable for measurements of the bulk E_F [15]. An alternative technique, which can be used to examine the position of E_F in TIs, is SdH [5]. This technique also provides an opportunity to determine a wide range of transport parameters of the bulk as well as of TSS. The observation of SdH oscillations in Sb_2Te_2Se has been published in several reports [16-18]. The Berry phase, determined from the data, demonstrated that such oscillations originate from TSS.

Despite the stability of TSS in Sb_2Te_2Se against air exposure and extrinsic doping, individual measurements on different samples by different techniques often do not achieve consistency. For example, values for the Fermi wave vector $k_F = 0.065$ $Å^{-1}$ and Fermi velocity $v_F = 5.5 \cdot 10^5$ m/s [13] obtained by ARPES are significantly different from the SdH values of $k_F = 0.08$ $Å^{-1}$ and $v_F = 6.7 \cdot 10^5$ m/s [17], $k_F = 0.08$ $Å^{-1}$ and $v_F = 7.9 \cdot 10^5$ m/s [18]. The reason may be different methods and conditions of crystal growth (the resistance-heated floating zone furnace [13] and the Bridgman [17,18] methods). To the best of our knowledge no comparison of the results of SdH analysis with ARPES measurements, carried out on the same sample of Sb_2Te_2Se, has been reported as yet.

Topological insulators have mostly been examined with respect to their surface states. However, recent publications reveal novel unconventional phenomena related to thermoelectric effects mostly related to the electronic band structure in the bulk in general and the nature and position of the bandgap in the Brillouin zone in particular [19]. The band structure of Sb_2Te_2Se has been examined theoretically, using *ab initio* approaches [6,12]. The bulk dispersion relations at the Γ point in these reports propose a "camel-back" shape for both the bulk valence and conduction bands. Due to the *p*-type conductivity of the examined samples such a shape was verified experimentally (using ARPES) only for the valence band [13]. To the best of our knowledge the reported studies revealed neither the shape of the dispersion relations for the bulk conduction band, the bandgap width (E_g) nor its nature (if the bandgap is direct or indirect). An alternative technique to examine the electronic band structure is the optical spectroscopy [20]. This technique has been successfully used to identify the nature of the bandgap and to measure its magnitude in the three model binary TIs: Bi_2Se_3 [21], Bi_2Te_3 [22] and Sb_2Te_3 [23].

Experimental estimates of E_g, determined from optical transmission spectra of Sb_2Te_2Se, are scattered from 0.37 eV [24] to 0.42 eV [13] at low temperatures whereas for 296 K the bandgap was estimated to be of 0.34 eV [13]. It still remains unclear whether Sb_2Te_2Se is a direct or indirect bandgap material and where in the Brillouin zone the bandgap can be located.

In this report we present a comprehensive study of the bulk crystalline sample of the topological insulator Sb_2Te_2Se, grown by the vertical Bridgman technique. The elemental composition, structural, optical and magneto-optical properties as well as the electronic structure of the same sample were examined by energy-dispersive X-ray spectroscopy (EDX), powder X-ray Diffraction (XRD), Raman, mid-infrared (MIR) optical magneto-transmission, ARPES and SdH techniques, respectively.

*Contact author: yulya.khatchenko@mail.ru

II. METHODS

A flat 3×3 mm^2 free standing sample with a thickness of 3 mm was cut perpendicular to the *c*-axis and along the hexagonal planes (0001) from the middle part of a bulk crystalline ingot grown in a sealed carbon coated quartz ampoule by the vertical Bridgman technique from a mix of the 4 N or 5 N purity elements Sb, Te and Se [25].

The elemental composition of the sample was measured by EDX analysis carried out using an Inspect F (FEI) scanning electron microscope. The component homogeneity was examined by EDX measurements at several points across the surface of the sample.

Phase purity and crystal structure of the grown material were examined XRD measurements at room temperature employing a Shimadzu XRD-7000 Maxima diffractometer (Cu Kα radiation, graphite monochromator, with the 2θ range from 5° to 95°, 0.02° step and a counting time of 12 s per step).

Polarisation resolved Raman measurements were performed in the backscattering geometry from the crystal basal plane using a RM1000 Renishaw micro-Raman spectrometer equipped with 532 nm solid-state and 633 nm helium-neon lasers. The "parallel" polarisation geometry (with the polarisation of the scattered light parallel to that of the incident light, XX) and the perpendicular one (with the polarization of scattered light perpendicular to the polarization of incident light, XY) were both used. The laser power density was held below 1 mW/cm^2 to avoid heating the sample. A set of three volume Bragg gratings was used to analyze scattered light at near-zero frequencies.

MIR optical transmission and magneto-transmission measurements were carried out with light propagating along the *c* axis from 0.1 to 0.5 eV at 4.2 and 300 K using a Bruker IFS 66v/S Fourier transform spectrometer with a globar light source, light-pipe optics and a silicon composite bolometer as the detector. Magnetic fields up to 11 T, generated by a superconducting magnet and applied in the Faraday configuration with $\boldsymbol{B}$ perpendicular to the (0001) plane, were used to carry out the MIR magneto-transmission measurements at the Laboratoire National des Champs Magnétiques Intenses in Grenoble, France. For the transmission measurements films with a thickness of 10 μm were exfoliated from the surface of the Sb_2Te_2Se bulk crystal then placed on copper foils with 1×1 mm^2 holes cut at the center.

ARPES measurements were performed along the $\bar{\Gamma}-\bar{M}$ and $\bar{\Gamma}-\bar{K}$ directions of the Brillouin zone at about 80 K and pressure below 10^{-10} mbar using a SPECS ProvenX-ARPES system equipped with a UV-300 duoplasmatron type discharge UV light source ($h\nu$ = 21.22 eV) and ASTRAIOS 190 hemispherical electron energy analyzer at the Rzhanov Institute of Semiconductor Physics in Novosibirsk. The sample was cleaved under vacuum at room temperature. Low energy electron diffraction was used to characterize the long-range crystalline order as well as to determine high symmetry directions.

Magneto-transport measurements were carried out at the Atomic Institute of the Vienna University of Technology (TU Wien, Austria) using a 17 T superconducting magnet. Six contacts were soldered along the perimeter of a 0.28 mm thick rectangular plate, cleaved from the bulk crystal perpendicular to the *c* axis, to form a Hall bar structure. The longitudinal ρ_{xx} and Hall resistivity ρ_{xy} were measured using the conventional dc method (see e.g [26]) in magnetic fields $\boldsymbol{B}$ applied perpendicular to the (0001) hexagonal plane.

III. RESULTS

A. Energy dispersive X-ray microanalysis

The elemental composition 41.2 ± 0.8 at% of Sb, 39.2 ± 0.8 at% of Te and 19.6 ± 0.4 at% of Se, taken as the average of EDX measurements in 12 different points, suggested the chemical formula $Sb_{2.06}Te_{1.96}Se_{0.98}$ with a near stoichiometric selenium to tellurium ratio of [Se]/[Te] = 0.50 ± 0.02, and a 5% deficiency of the anions [Se + Te] over the cations [Sb].

B. X-ray diffraction

The experimentally measured powder XRD pattern for the grown crystals of Sb_2Te_2Se, a Rietveld refinement fit and the difference between the pattern and the fit as well as a standard set of Bragg reflections corresponding to the tetradymite structure are presented in Fig. 1. The GSAS-II package [27] was used for the crystal structure refinement by the Rietveld method.

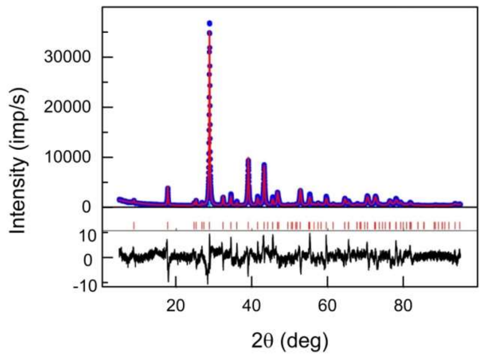

FIG 1. XRD pattern for Sb_2Te_2Se (blue circles), Rietveld fit (red line) and the difference between them (black line). Standard Bragg reflections for the tetradymite structure are shown by vertical red strokes.

C. Raman spectroscopy

Raman spectra of the pure A_{1g} (XX-XY geometry) and E_g (XY geometry) symmetries, measured at 300 K, are shown in Fig. 2(a).

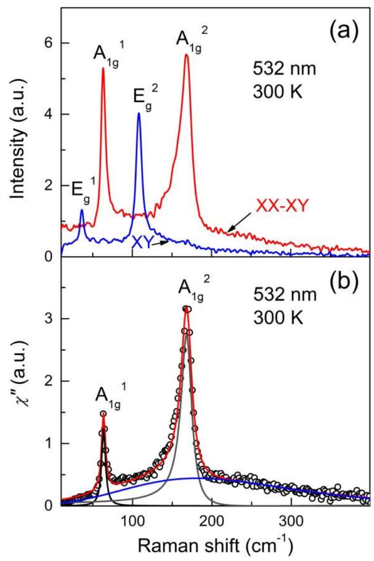

FIG 2. (a) Raman spectra taken at 300 K for the A_{1g} and E_g symmetries. (b) Raman susceptibility for the A_{1g} symmetry spectrum decomposed into excitation components.

*Contact author: yulya.khatchenko@mail.ru

Each spectrum demonstrates two sharp lines at 37 cm^{-1} and 108 cm^{-1} as well as 64 cm^{-1} and 162 cm^{-1} for the A_{1g} and E_g symmetries, respectively. The spectra also contain broad background features (continuum). To determine the Raman susceptibility χ"(ω) the A_{1g} spectrum was normalised by the Bose factor $[1-\exp(-\hbar\omega/kT)]^{-1}$ as shown in Fig. 2(b).

D. Optical transmission spectroscopy

The bandgap region of the MIR optical transmission spectra, measured at 4.2 and 300 K, is displayed in Fig. 3(a).

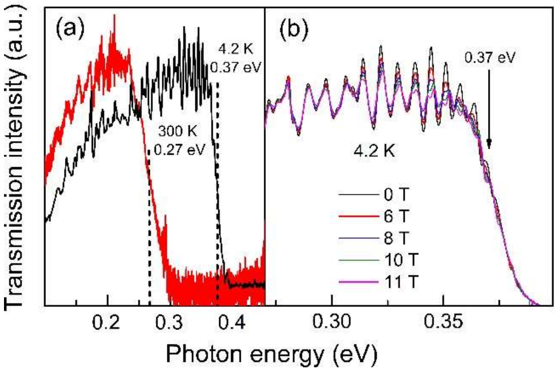

FIG 3. (a) Zero field MIR optical transmission spectra measured at 4.2 and 300 K. (b) The effect of magnetic fields on the transmission spectrum at 4.2 K.

The spectra show a sharp absorption band edge at 0.37 eV for the 4.2 K spectrum and 0.27 eV for the 300 K one estimated at the middle of the absorption edge. Both spectra reveal a significant intensity of Fabry-Perot (FP) oscillations showing that top and bottom surfaces of the sample are parallel. The effect of magnetic fields on the transmission spectra is shown in Fig. 3(b). The magnetic fields introduce no significant changes in the shape and spectral position of the absorption edge. However, the fields modify the FP oscillations attenuating their intensity.

E. Angle-resolved photoelectron spectroscopy

ARPES spectra of the Sb_2Te_2Se (0001) surface measured at 80 K are shown in Fig.4. Fig. 4(a) displays the band dispersions along the $\bar{\Gamma}-\bar{M}$ and $\bar{\Gamma}-\bar{K}$ directions of the Brillouin zone. At about 75 meV below E_F the bulk valence band reveals maxima at $k_{||} \approx 0.1$ Å^{-1} and at $k_{||} \approx 0.44$ Å^{-1} in the $\bar{\Gamma}-\bar{M}$ direction whereas in the $\bar{\Gamma}-\bar{K}$ direction a maximum of the valence band can also be seen at $k_{||} \approx 0.1$ Å^{-1} indicating a *p*-type conductivity of the sample surface. The topological surface states are clearly visible in the $\bar{\Gamma}-\bar{K}$ direction. Linear dispersions of the Dirac cone in this direction, shown in Fig. 4(a) by dashed lines, appear from a binding energy of 0.35 eV and extend to E_F at k_F = 0.083 Å^{-1}. Fig. 4(b) shows 2D constant energy maps at E_F and 75 as well as 150 meV below this level.

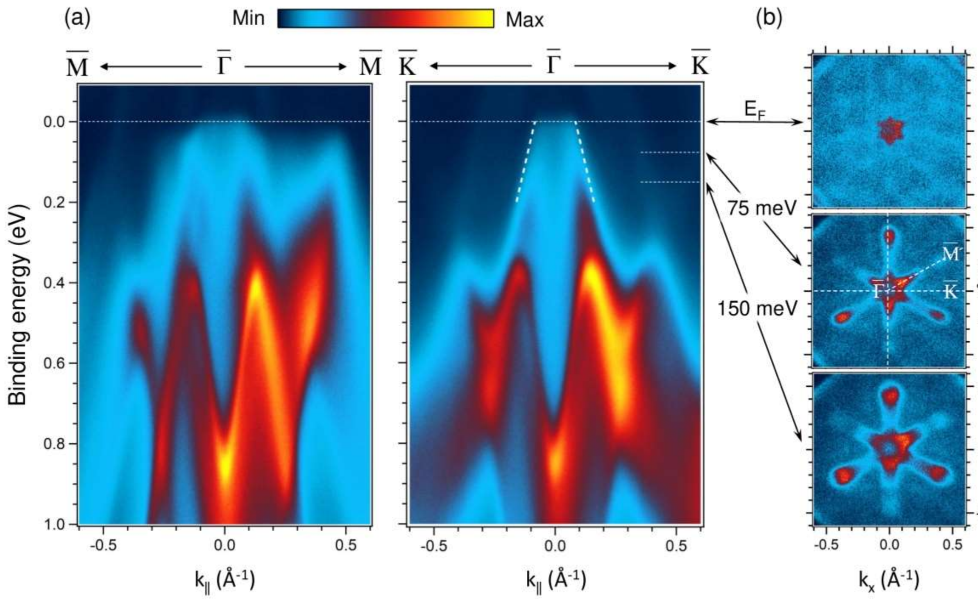

FIG 4. ARPES spectra of Sb_2Te_2Se at 80 K. (a) Band dispersions along the $\bar{\Gamma}-\bar{M}$ and $\bar{\Gamma}-\bar{K}$ directions. (b) Constant energy maps at the Fermi level, 75 and 150 meV ($h\nu$ = 21.22 eV).

*Contact author: yulya.khatchenko@mail.ru

At the Fermi surface one can see only a cross section of the Dirac cone. The bulk component of the band dispersions, appearing at 75 and 150 meV below in both the $\overline{\Gamma}-\overline{M}$ and $\overline{\Gamma}-\overline{K}$ directions, demonstrates a three-fold symmetry. A significant hexagonal warping due to the interference of the bulk bands with TSS can be seen in the constant energy maps.

F. Magneto-transport measurements

To complement the magneto-optical and ARPES experiments, magneto-transport measurements on the same sample have been carried out. Both transversal Hall (ρ_{xy}) and longitudinal (ρ_{xx}) components of the magneto-resistivity with magnetic field along the trigonal axis were measured.

The temperature dependence of the longitudinal component has also been examined. Fig. 5(a) shows ρ_{xx} as a function of temperature. The resistivity decreases with decreasing temperature revealing a typical metallic behaviour. At temperatures below 18 K, the resistivity slightly increases. A similar low temperature resistance upturn has been observed in thin film and bulk topological insulators [28-32] with the temperature of the resistance minimum varying from 8 K [28] to 30 K [30]. In non-magnetic topological insulators the upturn has been assigned to the two-dimensional effects of weak localization and electron-electron interaction (EEI) [28, 29, 32] as well as to increasing bulk resistivity due to localisation of bulk carriers on defects [32, 33]. To clarify the origin of the upturn we plotted the low temperature part of ρ_{xx} as a function of $T^{1/2}$, since a $T^{1/2}$ dependence has been associated with three-dimensional disorder-enhanced EEI [34-36]. The inset of Fig. 5(a), shows a clear linear behaviour, which leads us to infer that EEI is the dominant effect. Further support for this comes from the observation that the hole concentration increases slightly as the temperature reduces from 20 K to 4 K.

The magnetic field dependence of the longitudinal resistivity ρ_{xx} and Hall resistivity ρ_{xy} measured at 4.2 K are shown in Fig. 5(b). The Hall resistivity shows an almost linear behaviour in magnetic fields up to 10 T with a positive slope indicating the *p*-type conductivity of the samples, which is consistent with our ARPES data. The nonlinearity is attributed to the presence of several transport channels: at the surface and in the bulk [4]. The ρ_{xy} dependencies, measured at positive and negative directions of the magnetic field are near identical. The Hall coefficient measurements at $B = 5$ T revealed a hole concentration of $n_p = 4.9 \cdot 10^{19}$ cm^{-3} and a mobility of $\mu = 913$ cm^2/(V·s). Noticeable SdH oscillations can be seen in Fig.5 (b) at fields above 10 T.

IV. DISCUSSION

The 5% deficiency of [Se + Te] over [Sb] induces the formation of Te and Se vacancies (V_{Te} and V_{Se}), interstitials of Sb (Sb_i) as well as antisite defect complexes because the cations and anions in Sb_2Te_2Se have a similar electronegativity [37].

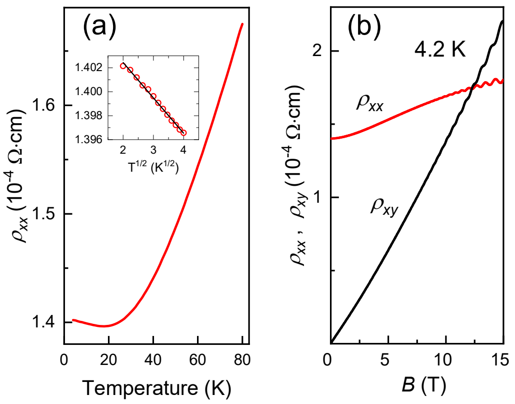

FIG 5(a). The temperature dependence of the longitudinal resistivity ρ_{xx}. The inset shows the low temperature dependence $\rho_{xx}(T^{1/2})$ and the best fitted straight line. (b) Magnetic field dependences of the longitudinal resistivity ρ_{xx} and Hall resistivity ρ_{xy} measured at 4.2 K.

Although the *p*-type conductivity of the sample some of these defects can be acceptors whereas others can be donors resulting in a degree of compensation. The Fermi level position and charge carrier concentration can be controlled by self-doping: changing the cation to anion ratio.

All the reflections in the experimental XRD pattern in Fig. 1, correspond only to the tetradymite structure [38, 39] revealing no signs of secondary phases. This manifests a high structural quality of the crystal whereas high intensity and small full width at half maximum of the main peaks of 0.1° in this pattern confirms the homogeneity of the material. The crystal structure corresponds to the space group $R\bar{3}m$ [40] with the unit cell parameters $a = 4.1854(3)$ Å, c = 29.924(1) Å and refined atomic positions: Sb (3m, 0 0 0.39422(4)), Te (3m, 0 0 0.78522(3)), Se ($\bar{3}$ m, 0 0 0) with the discrepancy factors $R_{\omega p} = 2.43\%$, $R_B = 4.42\%$ and the goodness of the fit $\chi^2 = 5.06$.

The symmetry group analysis of the $R\bar{3}m$ space group of Sb_2Te_2Se gives the following irreducible representation:

$$\Gamma_{ph} = 2A_{1g} + 2E_g + 3A_{2u} + 3E_u, \qquad (1)$$

*Contact author: yulya.khatchenko@mail.ru

where A_{1g} and E_g are Raman-active modes whereas the A_{1u} and E_u modes are infrared-active ones. The Raman tensors of optical phonons for the tetradymite structure allow the observation of both A_{1g} and E_g phonons in the XX geometry, while E_g phonons can only be observed in the XY geometry. Thus, measurements in these two geometries make it possible to determine the spectra of both the pure A_{1g} and E_g symmetries shown in Fig. 2(a). According to the selection rules the $2A_{1g}$ (at 64 and 168 cm^{-1}) and $2E_g$ (at 36 and 108 cm^{-1}) modes can be seen in these spectra under excitation by both laser lines. These results are consistent with earlier observations [41]. However, our spectra reveal a better signal-noise ratio providing more details in the spectra. It can be seen that the line shape of the high-frequency modes A_{1g}^2 and E_g^2 is asymmetric, suggesting interference of these modes with the continuum [42]. To improve the accuracy of interpretation of the experimental Raman susceptibility $\chi''(\omega)$ the phonon lines were fitted with Lorentzian (A_{1g}^1) and Breit-Wigner-Fano profiles (A_{1g}^2) and then superimposed with the broad asymmetric peak as shown in Fig. 2(b) [42]. This fitting helped to estimate the spectral position of the continuum peak maximum of 180 cm^{-1} and the asymmetry parameter for the A_{1g}^2 line Q = - 8. A similar decomposition of the E_g spectrum gives a lower energy of the continuum maximum of 130 cm^{-1} and the opposite sign of the asymmetry parameter Q = 12 for the E_g^2 line. The probable origin of such a continuum can be a high concentration of charge carriers resulting in electron-phonon scattering. In the case of a collisionless mechanism (at low temperatures), the energy of the continuum maximum can be estimated by the value of qv_F, where q is the probed wave vector whereas v_F is the Fermi surface electron velocity [43]. A probed wave vector of $5 \cdot 10^5$ cm^{-1}, for the visible range of light, and $v_F \sim 4 \cdot 10^7$ cm/s result in $qv_F \sim 105$ cm^{-1}. This estimate is smaller to the observed here energy of the continuum maximum. Spectra of electronic excitations with such energies have been reported for metals [44]. At room temperature the energy of electron-phonon scattering effects can be comparable with qv_F leading to an increase in the energy of the electron continuum. If these effects dominate, then the continuum energy is determined by the temperature-dependent carrier relaxation frequency. A better understanding of the nature of the observed scattering requires detailed measurements at low temperatures.

The E_g^2 and A_{1g}^2 modes in the Raman spectra of Sb_2Te_2Se are shifted to higher frequencies in comparison with Bi_2Te_2Se because Sb atoms are lighter than Bi ones. A similar shift was also observed after Bi atoms in Bi_2Te_2S were substituted with Sb converting this compound to Sb_2Te_2S [41]. In general, the observed phonon features additionally confirm the phase purity and the tetradymite structure of the examined material.

An accurate measurement of the bandgap E_g and establishing its character can be achieved by using the Tauc method [45]. The dependence of the absorption coefficient α on the photon energy $h\nu$ for a direct bandgap transition can be expressed by the following equation [46]:

$$\alpha h\nu = C(h\nu - E_g)^{1/2} \tag{2}$$

where C is a constant. At the bandgap photon energies absorption can be estimated by absorbance normalised by the thickness of the sample $\alpha \approx -ln(T)/d$ [47]. The $(\alpha h\nu)^2$ dependence on $h\nu$ is plotted in Fig.3(b) for both 4.2 K and 300 K assuming the direct and allowed nature of the transition. Both dependencies reveal clear linear regions. Such a linearity can be taken as an evidence that the bandgap is indeed direct. Straight lines were fitted into these linear regions as shown in Fig.6. The bandgap width of 0.377 ± 0.008 eV at 4.2 K and 0.242 ± 0.005 eV at 300 K were determined by extrapolating the lines to the photon energy axis.

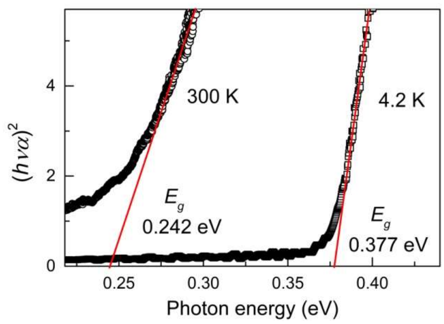

FIG 6. Linear parts of the $(\alpha h\nu)^2$ dependence on photon energy for transmission spectra measured at 4.2 K and 300 K with straight lines, fitted into the experimental data, extrapolated to the photon energy axis to determine the bandgap.

The observed red shift of the absorption edge as the temperature of the sample increases to 300 K follows the general semiconductor trend. According to first-principles calculations [48] such a bandgap reduction for the Bi_2Se_3 family of topological insulators can be attributed equally to thermal expansion and electron-phonon coupling. We can estimate the rate of shrinking of the band gap at increasing temperature assuming a linear dependence of E_g on temperature $E_g \approx 0.377 - 0.44 \cdot 10^{-4}\ T$, eV, which is similar to that for Bi_2Te_3 [22]. Assuming the 0.377 eV bandgap the energy position of the Dirac point at 0.22 eV above E_F was determined by extrapolating the dispersion lines

*Contact author: yulya.khatchenko@mail.ru

of TSS above the E_F in the $\overline{\Gamma}-\overline{K}$ branch as shown by dashed lines in Fig. 4(a). Thus, this point is located above E_F and is well away from the valence and conduction bands, fulfilling one of the necessary conditions for an application of topological insulators. The corresponding Fermi velocity was determined to be $v_F = 4.0 \cdot 10^5$ m/s.

The ARPES band dispersions in Fig. 4(a) suggest that the fundamental direct bandgap in Sb_2Te_2Se is not located at the zero-wave vector Γ point of the Brillouin zone. However, an alignment of the valence and conduction bands can be expected at a point close to Γ: at $k \approx 0.1$ Å^{-1} along either the $\overline{\Gamma}-\overline{M}$ or $\overline{\Gamma}-\overline{K}$ directions. According to the theoretical study [6] such an alignment should be along the $\overline{\Gamma}-\overline{K}$ directions of the Brillouin zone providing a theoretical estimate for the bandgap of 0.52 eV, which is comparable with our experimental value of 0.377 eV. Also, the theory predicts an indirect gap of 0.47 eV along the $\overline{\Gamma}-\overline{M}$ direction. The predicted in [6] band inversion region around the Dirac point includes the bandgap region.

Fig. 7(a) shows quantum oscillations of the longitudinal conductivity $\Delta\sigma_{xx}$ obtained by subtracting a smooth polynomial background from σ_{xx} calculated using the formula $\sigma_{xx} = \rho_{xx}/(\rho_{xx}^2 + \rho_{xy}^2)$ from the longitudinal ρ_{xx} and Hall ρ_{xy} resistivities.

The oscillations of $\Delta\sigma_{xx}$ are clear and periodic in $1/B$, suggesting the existence in Sb_2Te_2Se of a well-defined Fermi surface. Fig. 7(b) displays a single frequency of quantum oscillations at F = 225 T, obtained by taking a fast Fourier transform (FFT) of the quantum oscillations.

A Fermi wave vector of $k_F = 8.3\times10^6$ cm^{-1} was determined using the Onsager relation $F = \hbar k_F^2/(2e)$ assuming circular Fermi surface cross-sections. The Lifshitz-Kosevich (LK) equation [49] was used to fit the SdH oscillations:

$$\Delta\sigma_{xx} = A\frac{\lambda}{\sinh\lambda}\exp(-\lambda_D)\cos\left[2\pi\left(\frac{F}{B}+\frac{1}{2}-\beta\right)\right],$$

$$\lambda = \frac{2\pi^2 k_B T m_c}{\hbar eB}, \quad \lambda_D = \frac{2\pi^2 k_B T_D m_c}{\hbar eB}, \qquad (3)$$

where, A_0 is a constant, F is the frequency of the oscillations, B is the external magnetic field, β is the phase factor equal to the Berry phase divided by 2π, T is the sample temperature, T_D is the Dingle temperature and m_c is the effective (cyclotron) mass.

To determine the origin of the quantum oscillations, we find the phase factor β from the Landau level (LL) fan diagram as shown in Fig. 8. For Dirac fermions with the linear energy dispersions the phase factor should be β = 0.5 whereas for trivial fermions with parabolic energy dispersions β = 0 [50]. To construct the LL fan diagram shown in Fig. 8 inverse field positions of minima ($1/B_{min}$) and maxima ($1/B_{max}$) of $\Delta\sigma_{xx}$ were assigned to integer and half integer values, respectively. It can be seen from Eq. (3) that the N^{th} minimum of the oscillation occurs at the cosine arguments equals to π(2N−1). The slope of the N vs $1/B$ straight line corresponds to the oscillation frequency F whereas the intercept of this line extrapolated to the N-index axis gives the phase factor β, calculated as β = 1 – intercept. When fixing the slope at the frequency F, derived from the FFT analysis, β = 0.22 is obtained.

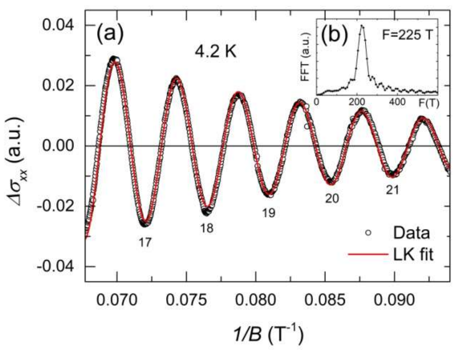

FIG 7. The oscillatory part of conductivity $\Delta\sigma_{xx}$ plotted as a function of the inverse magnetic field $1/B$ (open circles) and the Lifshitz-Kosevich fit (solid line). The minima positions are assigned as integer Landau level indices. The inset displays fast Fourier transform of $\Delta\sigma_{xx}$.

Deviations of β from 0.5 have been reported earlier and were attributed to a non-ideal shape of the Dirac cone and the Zeeman effect [51]. A Zeeman term, determining the spin coupling with the magnetic field, added to the Hamiltonian for non-ideal Dirac Fermions in TIs for magnetic fields perpendicular to the hexagonal plane (0001), accounts for a bending of the straight-line shape of the N on $1/B$ dependence at high B [52, 53]. The strength of the magnet used in our magneto-transport measurements was not sufficient to observe a possible non-linearity. On the other hand, the observed part of the Dirac cone, shown in Fig. 4(a), also does not provide an opportunity to evaluate the ideality of its shape. Never the less, we attribute the observed deviation of β to a non-ideal shape of the Dirac cone in our sample.

The LK fit to the SdH oscillations using the Eq. (3) is shown in Fig. 7(a) by the red solid line. In order to reduce the total number of free parameters in this equation, the frequency and phase factor were fixed at the values obtained from FFT analysis and LL fan diagram. With such a simplification we estimated a cyclotron effective mass of $m_c = 0.23m_0$ (m_0 is the free electron mass) and Dingle temperature T_D = 14.3 K.

*Contact author: yulya.khatchenko@mail.ru

The reported earlier effective masses scatter from $0.17m_0$ [16] to $0.1m_0$ [17,18]. Our estimate is larger than those reported earlier. This can be attributed to the simplification used to fit LK equation into the oscillatory part of conductivity $\Delta\sigma_{xx}$ plotted as a function of $1/B$ and/or to a non-ideal shape of the Dirac cone.

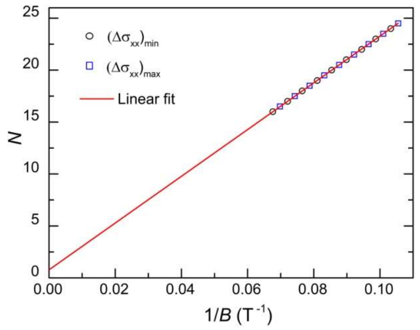

FIG 8. The Landau level (LL) fan diagram. The positions of minima and maxima in conductivity $\Delta\sigma_{xx}$ are shown by circles and squares, respectively. The solid line is the linear extrapolation of the linear fit to the data.

The Dingle temperature of 14.3 K is lower that reported in [17] and [18] but close to those reported in [16] and [14]. Knowing m_c and k_F we can calculate a Fermi velocity of $v_F = 4.2\cdot10^5$ m/s by using the formula $v_F = \hbar k_F/m_c$. A Fermi energy (relative to the Dirac point) of $E_F = 226$ meV, calculated as $E_F = m_c v_F^2$ assuming the case of Dirac fermions. The obtained values of k_F, v_F and E_F are in a good agreement with those determined from our ARPES data suggesting that the observed quantum oscillations indeed originate from the Dirac states and thus provide with a 2D surface carrier density n_{2D} of $5.4\cdot10^{12}$ cm^{-2} calculated as $n_{2D} = \pi k_F^2/(2\pi)^2$. The good consistency with the ARPES values also suggests that our ARPES measurements were not affected by band bending due to rather high charge carrier density. To check further the self-consistency of the determined parameters the Dingle temperature was also found from the magnetic field dependence of the oscillation amplitude. The slope of the straight line, fitted in the semilogarithmic plot of $\Delta\sigma_{xx}\cdot B\cdot sinh\lambda(T)$ vs $1/B$, shown in Fig. 9, resulted in a T_D value of 14.4 K which is almost identical to that determined by the fitting the LK equation.

The surface carrier life time $\tau = \hbar/2\pi k_B T_D$, mobility $\mu = e\tau/m_c$ and the mean free path $l = v_F\tau$ are estimated to be $\tau = 8.5\times10^{-14}$ s, $\mu = 648$ cm^2/(V·s) and $l = 35$ nm respectively. These parameters are quite close to those reported previously [17] and [18].

A simple two-band model, recently proposed to describe massive Dirac electrons in the bulk of topological insulators with a direct bandgap located at a non-Γ point of the Brillouin zone, was used to determine parameters of the electronic band structure of the bulk [22]. The Hamiltonian, developed in this model, was derived using the first-order $\boldsymbol{k}\cdot\boldsymbol{p}$ theory for non-zero but small momentum points in the Brillouin zone.

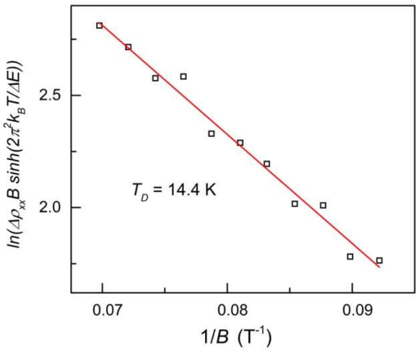

FIG 9. Dingle plot with the best linear fitting yielding the alternative value of the Dingle temperature.

Resulting dispersion relations for the conduction and valence bands are characteristic relativistic-like and hyperbolic $E(k) = \pm\sqrt{(E_g/2)^2 + \hbar^2 v_F^2 k^2}$. The dispersion relations display the full electron-hole symmetry whereas the bands are separated by a bandgap E_g. According to this model the electron and hole effective masses are equal to the Dirac mass which can be calculated using just two parameters (v_F and E_g) as $m_D = m_e = m_h = E_g/(2v_F^2)$. Assuming a Fermi velocity of $v_F = 4\cdot10^5$ m/s, determined in our ARPES measurements, the corresponding Dirac as well as the electron and hole masses were calculated $m_D = m_e = m_h = 0.21m_0$. This value is close to the mass of $0.23m_0$ determined for the Dirac fermions from our SdH experiments. However, according to the model [15] this bulk mass value is valid only at the very band edge whereas away from the band extrema the masses increase linearly with the momentum distance from the band edge $E(k) \approx \hbar v_F k$. According to the model, the magnitude of g factors for the valence and conduction bands are also equal and can be estimated as $|g_e| = |g_h| = 2m_0/m_D = 10$. This value is greater than $|g| = 6$ experimentally measured in Sb_2Te_2Se using scanning tunnelling microscopy [51]. However, both g-factor values are significantly smaller than $g_e = 28.5$, determined in Bi_2Se_3 [54]. Such a large g-factor results in a visible splitting of the absorption edge which was observed in the Bi_2Se_3 transmission spectra under the influence of magnetic fields [55] and provided an opportunity to experimentally estimate the magnitude of the g-factor in Bi_2Se_3. However, our transmission spectra, shown in Fig. 3(b), do not reveal any visible splitting under magnetic fields up to 11 T which supports the relatively moderate values of the g-factor magnitudes in Sb_2Te_2Se estimated from the above model.

*Contact author: yulya.khatchenko@mail.ru

V. CONCLUSIONS

A comprehensive study of the structural, magneto-optical and magneto-transport properties as well as the electronic band structure of the same sample of a *p*-conductivity type Sb_2Te_2Se bulk crystal, grown by the vertical Bridgman technique, was carried out.

The XRD and Raman spectroscopy showed a high structural quality and free from secondary phases tetradymite lattice structure with the $R\overline{3}m$ space group symmetry and lattice parameters $a = 4.1854(3)$ Å, $c = 29.924(1)$ Å. The asymmetric shape of the phonon lines and the presence of electronic light scattering demonstrate a significant electron-phonon interaction in the studied material.

MIR optical transmission spectra, measured at 4.2 K and 300 K, showed a sharp fundamental absorption edge. A bandgap of 0.377 eV at 4.2 K and 0.267 eV at 300 K was determined. The direct character of the bandgap was demonstrated. The shrinking of the gap with the temperature increase was attributed to the thermal expansion of the lattice and electron-phonon coupling.

ARPES measurements revealed a single Dirac cone confirming the topological insulator nature of the examined material. The Dirac point was found to be at 0.22 eV above E_F, within the bandgap and well away from the valence and conduction bands. The bandgap is likely to be not in the Γ point but at $k \approx 0.1$ Å^{-1} along the $\overline{\Gamma} - \overline{K}$ directions of the Brillouin zone.

Magneto-transport measurements revealed a metallic behaviour of bulk charge carriers along with the presence of single frequency SdH oscillations associated with the Dirac state. The non-trivial origin of the oscillations was demonstrated by a non-zero phase factor of $\beta = 0.22$.

All the measurements were carried out on the same sample. The consistency of SdH and ARPES results allowed us to overcome inconsistencies in earlier reports on this material using these techniques on different samples. In our work, the strong agreement the ARPES- and SdH-determined parameters of the electronic structure (k_F, v_F, E_F) is direct evidence that the observed SdH quantum oscillations indeed originate from the Dirac states, while the phase factor β deviates from 0.5 probably due to the non-ideal Dirac dispersion.

The combination of the direct bandgap nature, demonstrated by optical transmission data, with the non-Γ bandgap location, determined in ARPES, allowed us to apply a simple two-band model to calculate equal electron and hole effective masses $m_e \approx m_h \approx 0.21 m_0$ and g factors $g_e \approx g_h \approx 10$.

ACKNOWLEDGMENTS

The work was carried out within the framework of the state assignment of the Ministry of Science and Higher Education of the Russian Federation for the IMP UB RAS. Yu.E. Kovalenko thanks M.N. Miheev Institute of Metal Physics of UB RAS for supporting her study on the state assignment, which was carried out within the youth project of the IMP UB RAS No. m32-23. V.V. Marchenkov is grateful to Prof. H.W. Weber for a possibility to carry out the magneto-transport measurements at the Atomic Institute (TU Wien, Austria). XRD study was carried out within the state assignment for IMET UB RAS of Ministry of Science and Higher Education of the Russian Federation. ARPES study was carried out within the RSF Grant No. 25-62-00004. The work of V.A. Golyashov and O.E. Tereshchenko was carried out within the state assignment of the SRF «SKIF» Boreskov Institute of Catalysis of SB RAS (FWUR-2024-0040). Crystal growth was performed under state assignment of IGM SB RAS No.122041400031-2. The authors acknowledge the support of the LNCMI-CNRS in Grenoble as a member of the European Magnetic Field Laboratory (EMFL). The UK authors are grateful for the travel expenses reimbursement projects EP/X020304/1 and NS/A000060/1.

CRediT authorship contribution statement

Yulia E. Kovalenko: Writing – original draft, Writing – review & editing, Visualization, Investigation, Formal analysis, Conceptualization.
Michael V. Yakushev: Writing – original draft, Writing – review & editing, Methodology, Investigation, Conceptualization.
Vladimir I. Grebennikov: Writing – review & editing.
Vladimir A. Golyashov: Investigation, Writing – original draft.
Vyacheslav V. Marchenkov: Investigation, Writing – original draft.
Milan Orlita: Investigation.
Yuri S. Ponosov: Investigation, Writing – original draft.
Evgeniy I. Patrakov: Investigation.
Svetlana G. Titova: Investigation, Writing – original draft.
Robert W. Martin: Writing – review & editing.
Konstantin A. Kokh: Writing – review & editing, Resources.
Oleg E. Tereshchenko: Writing – review & editing, Resources.
Tatyana V. Kuznetsova: Writing – review & editing, Supervision, Project administration, Conceptualization.

*Contact author: yulya.khatchenko@mail.ru

[1] L. Fu and C. L. Kane, Superconducting Proximity Effect and Majorana Fermions at the Surface of a Topological Insulator, Phys. Rev. Lett. 100, 096407 (2008).

[2] J. E. Moore, The birth of topological insulators, Nature (London) 464, 194 (2010).

[3] M. Z. Hasan and C. L. Kane, Topological insulators, Rev. Mod. Phys. 82, 3045 (2010).

[4] Zhi Ren, A. A. Taskin, Satoshi Sasaki, Kouji Segawa, Yoichi Ando, Large bulk resistivity and surface quantum oscillations in the topological insulator Bi_2Te_2Se, Phys. Rev. B 82, 241306 (R) (2010).

[5] J. G. Analytis, R. D. McDonald, S. C. Riggs, J.-H. Chu, G. S. Boebinger and I. R. Fisher, Two-dimensional surface state in the quantum limit of a topological insulator, Nature Physics 6 (12), 960 (2010).

[6] H. Lin, T. Das, L. A. Wray, S.-Y. Xu, M. Z. Hasan, and A. Bansil, An isolated Dirac cone on the surface of ternary tetradymite-like topological insulators, New Jour. Phys. 13, 095005 (2011).

[7] M. Neupane, S.-Y. Xu, L.A. Wray, A. Petersen, R. Shankar, N. Alidoust, C. Liu, A. Fedorov, H. Ji, J.M. Allred *et al*., Topological surface states and Dirac point tuning in ternary topological insulators, Phys. Rev. B 85, 235406 (2012).

[8] T. Arakane, T. Sato, S. Souma, K. Kosaka, K. Nakayama, M. Komatsu, T. Takahashi, Zhi Ren, Kouji Segawa and Yoichi Ando, Tunable Dirac cone in the topological insulator $Bi_{2-x}Sb_xTe_{3-y}Se_y$, Nature Comm. 3, 636 (2012).

[9] M. V. Filianina, I.I. Klimovskikh, I.A. Shvets, A.G. Rybkin, A.E. Petukhov, E.V. Chulkov, V.A. Golyashov, K.A. Kokh, O.E. Tereshchenko, C. Polley *et al*., Spin and electronic structure of the topological insulator $Bi_{1.5}Sb_{0.5}Te_{1.8}Se_{1.2}$, Materials Chemistry and Physics 207, 253 (2018).

[10] N. P. Stepina, A. O. Bazhenov, A. V. Shumilin, A. Yu. Kuntsevich, V. V. Kirienko, E. S. Zhdanov, D. V. Ishchenko, and O. E. Tereshchenko, Indication for an anomalous magnetoresistance mechanism in $(Bi,Sb)_2(Te,Se)_3$ three-dimensional topological insulator thin films, Phys. Rev. B 108, 115401 (2023).

[11] I. V. Zhevstovskikh, Y. S. Ponosov, S. G. Titova, N. S. Averkiev, V. V. Gudkov, M. N. Sarychev, T. V. Kuznetsova, K. A. Kokh, and O. E. Tereshchenko, Anomalous behavior of the elastic and optical properties in $Bi_{1.5}Sb_{0.5}Te_{1.8}Se_{1.2}$ topological insulator induced by point defects, Phys. Status Solidi (b) 255, 1800264 (2018).

[12] S. Xu, L. A. Wray, Y. Xia, R. Shankar, A. Petersen, A. Fedorov, H. Lin, A. Bansil, Y. S. Hor, D. Grauer *et al*., Discovery of several large families of Topological Insulator classes with backscattering-suppressed spin-polarized single-Dirac-cone on the surface, arXiv:1007.5111

[13] C. K. Lee, C. M. Cheng, S. C. Weng, W. C. Chen, K. D. Tsuei, S. H. Yu, M. M. C. Chou, C. W. Chang, L. W. Tu, H. D. Yang *et al*., Robustness of a topologically protected surface state in a Sb_2Te_2Se single crystal, Sci. Rep. 6, 36538 (2016).

[14] D. Mallick, Sh. Mandal, R. Ganesan, and P. S. Anil Kumar, Fermi level tuning and the robustness of topological surface states against impurity doping in Sn doped Sb_2Te_2Se, Appl. Phys. Lett. 118, 154001 (2021)

[15] J. G. Analytis, J.-H. Chu, Yu. Chen, F. Corredor, R. D. McDonald, Z. X. Shen and Ian R. Fisher, Bulk Fermi surface coexistence with Dirac surface state in Bi_2Se_3: A comparison of photoemission and Shubnikov–de Haas measurements, Phys. Rev. B 81, 205407 (2010).

[16] S.-M. Huang, Y.-J. Yan, S.-H. Yu and M. Chou, Thickness-dependent conductance in Sb_2SeTe_2 topological insulator nanosheets, Scientific Reports 7, 1 (2017).

[17] K. Shrestha, V. Marinova, D. Graf, B. Lorenz, and C. W. Chu, Quantum oscillations in metallic Sb_2Te_2Se topological insulator, Phys. Rev. B 95, 075102 (2017)

[18] G. Govindhan, E. P. Amaladass, A. B. Govindan, G. Sarveswaran, A. Mani, Studies on Shubnikov-de Hass oscillations in p-Sb_2Te_2Se topological insulator, Materials Research Bulletin 124, 110733 (2020)

[19] M. Y. Toriyama and G. J. Snyder, Topological insulators for thermoelectrics: A perspective from beneath the surface, The Innovation 6(3), 100782 (2025)

[20] P. Y. Yu and M. Cardona, *Fundamentals of Semiconductors: Physics and Materials Properties* (Springer, Berlin, 1996).

[21] M. Orlita, B. A. Piot, G. Martinez, N. K. S. Kumar, C. Faugeras, M. Potemski, C. Michel, E. M. Hankiewicz, T. Brauner, Č. Drašar *et al*., Magneto-Optics of Massive Dirac Fermions in Bulk Bi_2Se_3, Phys. Rev. Lett. 114, 186401 (2015).

[22] I. Mohelský, A. Dubroka, J. Wyzula, A. Slobodeniuk, G. Martinez, Y. Krupko, B. A. Piot, O. Caha, J. Humlíček, G. Bauer *et al*., Landau level spectroscopy of Bi_2Se_3, Phys. Rev. B 102, 085201 (2020).

[23] I. Mohelsky, J. Wyzula, F. Le Mardelé, F. Abadizaman, O. Caha, A. Dubroka, X. D. Sun, C. W. Cho, B. A. Piot, M. F. Tanzim *et al*., Electronic band structure of Sb_2Te_3, Phys. Rev. B 109, 165205 (2024).

[24] Yu.E. Kovalenko, M.V. Yakushev, V.I. Grebennikov, M. Orlita, S.G. Titova, K.A. Kokh, O.E. Tereshchenko, T.V. Kuznetsova, Electronic properties of the topological insulator Sb_2Te_2Se, Semiconductors 58 (4), 185 (2024).

[25] O. E. Tereshchenko, K. A. Kokh, V.V. Atuchin, K. N. Romanyuk, S. V. Makarenko, V. A. Golyashov, A. S. Kozhukhov, I. P. Prosvirin and A. A. Shklyaev, Stability of the (0001) surface of the Bi_2Se_3 topological insulator, JETP Letters 94 (6), 465 (2011).

[26] A.N. Cherepanov, V.V. Marchenkov, V.E. Startsev, N.V. Volkenstein, M. Glinski, High-field galvanomagnetic properties of compensated metals

*Contact author: yulya.khatchenko@mail.ru

under electron-surface and intersheet electron-phonon scattering (tungsten), J. of Low Temp. Phys. 80, 135 (1990).

[27] B.H. Toby and R.B. Von Dreele, GSAS-II: The Genesis of a Modern Open-Source All Purpose Crystallography Software Package, J. Appl. Cryst. 46, 544 (2013).

[28] E. Osmic, J. Barzola-Quiquia, S. Winnerl, W. Böhlmann and P. Häussler, Thermopower and resistivity of the topological insulator Bi_2Te_3 in the amorphous and crystalline phase, J. Phys.: Condens. Matter 36, 355001 (2024)

[29] J. Wang, A. M. DaSilva, C. Chang, Ke He, J. K. Jain, N. Samarth, X.-C. Ma, Q.-K. Xue, and M. H. W. Chan, Evidence for electron-electron interaction in topological insulator thin films, Phys. Rev. B 83, 245438 (2011)

[30] N. P. Butch, K. Kirshenbaum, P. Syers, A. B. Sushkov, G. S. Jenkins, H. D. Drew, and J. Paglione, Strong surface scattering in ultrahigh-mobility Bi_2Se_3 topological insulator crystals, Phys. Rev. B 81, 241301 R (2010)

[31] K. Wang, D. Graf, and C. Petrovic, Large magneto-thermopower and Fermi surface reconstruction in Sb_2Te_2Se, Phys. Rev. B, 89(12), 125202 (2014)

[32] R. K. Gopal, S. Singh, A. Mandal, J. Sarkar & C. Mitra, Topological delocalization and tuning of surface channel separation in Bi_2Se_2Te Topological Insulator Thin Films, Sci. Rep. 7, 4924 (2017)

[33] M.D. Anoop, Jyoti Yadav, Nisha Yadav, Rini Singh, K. Shinzato, S.N. Dolia, Ankur Jain, T. Ichikawa, Manoj Kumar, Effect of isovalent substitution on the structural and electrical properties of $Bi_xSb_{2-x}Te_3$ topological insulator single crystals, Materials Today: Proceedings 31, 616 (2020)

[34] L.J. Zhu, J.H. Zhao, Anomalous resistivity upturn in epitaxial $L2_1$-Co_2MnAl films, Sci. Rep. 7, 42931 (2017)

[35] Shucheng Tong, Xupeng Zhao, Dahai Wei, and Jianhua Zhao, Low-temperature resistivity anomaly and weak spin disorder in Co_2MnGa epitaxial thin films, Phys. Rev. B, 184434 (2020)

[36] B.L. Altshuler, A.G. Aronov. Contribution to the theory of disordered metals in strongly doped semiconductors, Sov. Phys. JETP 50 (5), 968 (1979)

[37] M. R. Diznab, I. Maleki, S. M. Vaez Allaei, Y. Xia and S. S. Naghavi, Achieving an ultrahigh power factor in Sb_2Te_2Se monolayers via valence band convergence, ACS Applied Materials 11 (50), 46688 (2019).

[38] H. Ji, J. M. Allred, M. K. Fuccillo, M. E. Charles, M. Neupane, L.A. Wray, M. Z. Hasan, and R. J. Cava, $Bi_2Te_{1.6}S_{1.4}$: A topological insulator in the tetradymite family, Phys. Rev. B 85, 201103(R) (2012).

[39] D. Harker, The crystal structure of the mineral tetradymite, Bi_2Te_2S, Z. Kristallogr. 89, 175 (1934).

[40] T. L. Anderson and H. B. Krause, Refinement of the Sb_2Te_3 and Sb_2Te_2Se structures and their relationship to nonstoichiometric $Sb_2Te_{3-y}Se_y$ compounds, Acta Cryst. B30, 1307 (1974).

[41] V. Chis, I. Y. Sklyadneva, K. A. Kokh, V. A. Volodin, O. E. Tereshchenko and E. V. Chulkov, Vibrations in binary and ternary topological insulators: First-principles calculations and Raman spectroscopy measurements, Phys. Rev. B 86 (17), 174304 (2012).

[42] M.V. Klein, in *Light Scattering in Solids*, edited by M. Cardona, (Springer-Verlag, Berlin, 1975), p. 174.

[43] Yu. S. Ponosov and S. V. Streltsov, Measurements of Raman scattering by electrons in metals: The effects of electron-phonon coupling, Phys. Rev. B 86, 045138 (2012).

[44] Yu.S. Ponosov and S.V. Streltsov, Q-Dependent Light Scattering by Electrons in LaB_6, JETP Letters 97 (8), 447 (2013).

[45] J. Tauc, R. Grigorovici, A. Vancu, Optical Properties and Electronic Structure of Amorphous Germanium, Phys. Status Solidi B 15, 627 (1966).

[46] J. I. Pankove, *Optical Processes in Semiconductors* (Courier Corporation, Massachusetts, 1971).

[47] G. Martinez, B.A Piot, M. Hakl, M. Potemski, Y.S. Hor, A. Materna, S.G. Strzelecka, A. Hruban, O. Caha, J. Novák *et al*., Determination of the energy band gap of Bi_2Se_3, Sci. Rep. 7, 6891 (2017).

[48] B. Monserrat, D. Vanderbilt, Temperature effects in the band structure of topological insulators, Phys. Rev. Lett. 117 (22), 226801 (2016).

[49] D. Shoenberg, *Magnetic Oscillations in Metals* (Cambridge University Press, Cambridge, 1984).

[50] Y. Ando, Topological Insulator Materials, J. Phys. Soc. Jpn. 82, 102001 (2013).

[51] Y-S Fu, T Hanaguri, K Igarashi, M Kawamura, M S Bahramy, T. Sasagawa, Observation of Zeeman effect in topological surface state with distinct material dependence, Nat. Commun. 7, 10829 (2016).

[52] A. A. Taskin and Y. Ando, Berry phase of nonideal Dirac fermions in topological insulators, Phys. Rev. B 84 (3), 035301 (2011).

[53] Y. Pan, A.M. Nikitin, D. Wu, Y.K Huang, A. Puri, S. Wiedmann, U. Zeitler, E. Frantzeskakis, E. Van Heumen, M.S. Golden, A. De Visser, Quantum oscillations of the topological surface states in low carrier concentration crystals of $Bi_{2-x}Sb_xTe_{3-y}Se_y$, SSCom 227, 13 (2016).

[54] A. Wolos, A. Drabinska, S. Szyszko, M. Kaminska, S. G. Strzelecka, A. Hruban, A. Materna, and M. Piersa, Three-dimensional topological insulators Bi_2Te_3, Bi_2Se_3, and Bi_2Te_2Se - a microwave spectroscopy study, AIP Conf. Proc. 1566, 197 (2013).

[55] L. Ohnoutek, M. Hakl, M. Veis, B.A. Piot, C. Faugeras, G. Martinez, M.V. Yakushev, R.W. Martin, Č. Drašar, A. Materna *et al*., Strong interband Faraday rotation in 3D topological insulator Bi_2Se_3, Sci. Rep. 6:19087 (2016).

*Contact author: yulya.khatchenko@mail.ru